JOURNAL OF COMPUTATIONAL PHYSICS **127,** 227–245 (1996)
ARTICLE NO. 0172

Coupling Boltzmann and Navier–Stokes Equations by Friction

JEAN-FRANÇOIS BOURGAT,*[,1] PATRICK LE TALLEC,†[,2] AND MOULAY D. TIDRIRI‡[,3]

*INRIA, Domaine de Voluceau- Rocquencourt- B.P. 105- Le Chesnay Cedex, France; †Université Paris-Dauphine and INRIA, Domaine de Voluceau- Rocquencourt- B.P. 105- Le Chesnay Cedex, France; ‡ICASE, Mail Stop 132C, Hampton, Virginia 23681-0001

Received February 27, 1995; revised December 18, 1995

The aim of this paper is to introduce and validate a coupled Navier–Stokes Boltzman approach for the calculation of hypersonic rarefied flows around manoeuvering vehicles. The proposed strategy uses locally a kinetic model in the boundary layer coupled through wall friction forces to a global Navier–Stokes solver. Different numerical experiments illustrate the potentialities of the method.

1. INTRODUCTION

Computing flows around manoeuvering vehicles at high altitudes involve different regimes, characterized by the so-called Knudsen number Kn. This adimensional number measures the ratio between the average time separating two successive collisions of a given particle and a characteristic time of the external flow. At altitudes of 70 km or below, this Knudsen number is very small and the flows are described by the Navier–Stokes equations. It is well known that Navier–Stokes equations cease to be valid for higher altitudes corresponding to Knudsen numbers larger than 10^{-3}. At this level, slip effects can be observed in the boundary layer and the gas gets rarefied in the wake. For example, such slip effects can be observed in Fig. 1, where a kinetic calculation carried over a wedge plate at high Mach number predicts a tangential velocity at the wall of the order of 100 m/s for a velocity at infinity equal to 1477 m/s. Such effects can lead to significant changes in the aerodynamic coefficients of the vehicle.

The standard solution is to use analytical slip boundary conditions as described in [11, 7, 28]. But the constants which are involved are hard to identify and their validity is questionable. On the other hand, a direct simulation of the kinetic problem is rapidly too expensive, because it requires one computational cell per mean free path. To overcome such difficulties, many authors have recently tried to use intermediate asymptotic models such as Burnett equations [29].

The solution proposed herein is quite different. It uses locally a kinetic model in the boundary layer coupled to a global Navier–Stokes solver. The coupled problem is solved by the time marching algorithm introduced and studied in [14, 25]. The coupling can be achieved either by friction (present work) or by half fluxes [3]. A complete analysis of the coupling strategy, summarizing and developing the results obtained in the phase research and development of the European space program Hermès is described in [25]. In [25], the model used to solve Boltzmann equation is simply the hard sphere model and for Navier–Stokes the viscosity is assumed to be constant, while in the present work more sophisticated physical models on both the viscosity and internal energy are used which turn out to be very important when trying to recover experimental results. In Section 2, we describe the kinetic governing equation with an emphasis on the transition regime, followed in Section 3 by a brief description of the Navier–Stokes equations. In Section 4, we describe the coupling strategy. The following section describes the global Navier–Stokes solver. The numerical method used to solve the Boltzmann equation is introduced in Section 6. Numerical results are presented in Section 7. And finally, we end this paper by concluding remarks.

2. BOLTZMANN EQUATION

Let f be the density of gas particles at position x with velocity v, and internal energy I. The Boltzmann equation of rarefied gas dynamics characterizes this density as the solution of the integrodifferential equation [8]

$$\frac{\partial f}{\partial t} + v\,\frac{\partial f}{\partial x} = Q(f,f).$$

[1] Email: Jean.Bourgat@inria.fr.
[2] Email: Patrick.LeTallec@inria.fr.
[3] Email: tidriri@icase.edu. This work was started in 1991 at INRIA and has been supported by the Hermes Research program under Grant RDAN 86.1/3. Partial support of CEA-CESTA is also gratefully acknowledged. Special thanks are also due to F. Mallinger and B. Mohammadi for their contribution to the numerical tests.

0021-9991/96 $18.00

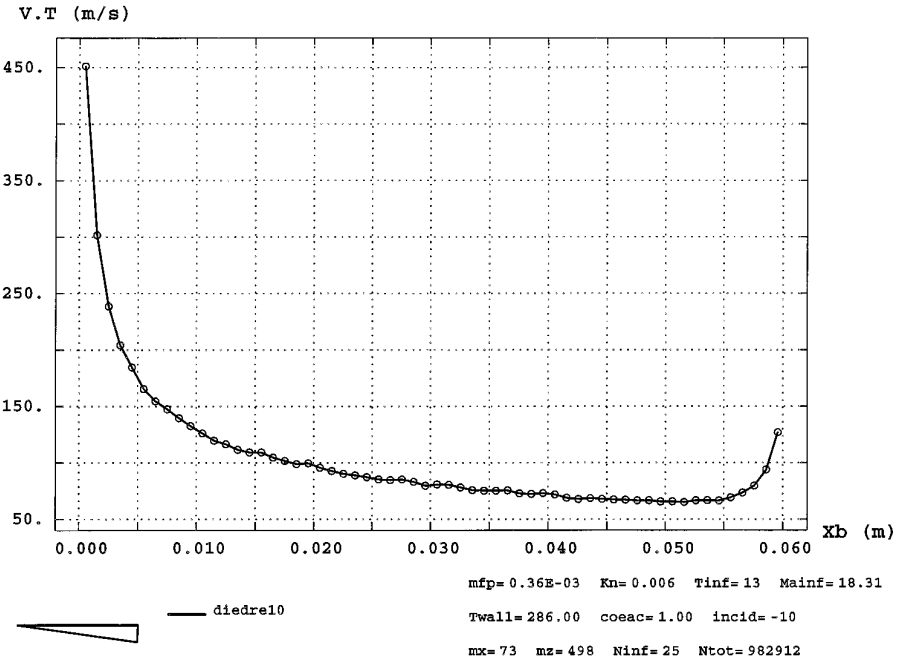

FIG. 1. Slip velocity on a flat plate as predicted by a kinetic simulation.

For molecular gas having internal degrees of freedom, the collision operator Q is defined by

$$Q(f,f) = \int_{\Delta} \left(f' f'_* \left(\frac{II_*}{I'I'_*} \right)^{\delta-1} - ff_* \right) B dv_* dI_* \varphi_\delta(r) dr \psi_\delta(R) dR d\omega,$$

with

$$\Delta = \mathbb{R}^3 \times \mathbb{R}_+ \times [0,1]^2 \times S^2$$
$$\varphi_\delta(r) = [r(1-r)]^{\delta/2-1}, \quad \psi_\delta(R) = R^2(1-R^2)^{\delta-1}.$$

As usual we have used the notation $f = f(v, I)$, $f' = f(v', I')$, $f_* = f(v_*, I_*)$ ..., with (v_*, I_*) the velocity and internal energy of the colliding particle, and (v', v'_*) and (I', I'_*) the postcollision velocities and internal energies. As in the monoatomic case, in a given collision, the collision direction $\omega \in S^2$ is fixed and we transform the vector (v, v_*, I, I_*) with $v, v_* \in \mathbb{R}^3$, $I, I_* \geq 0$, by setting

$$e^2 = \tfrac{1}{4}|v - v_*|^2 + I^2 + I_*^2 = \text{total energy of the collision},$$
$$g = v - v_* = \text{relative velocity},$$

and by defining the post collision velocities (v', v'_*) and energies (I', I'_*) by

$$v' + v'_* = v + v_*,$$
$$g' = v' - v'_* = 2Re\{g - 2\omega g.\omega\}/|g|,$$
$$I'^2 = r(1-R^2)e^2, \quad I'^2_* = (1-r)(1-R^2)e^2.$$

The factors R, $r \in [0, 1]$ introduced in the collision operator determine the quantity of energy which is exchanged between internal and kinetic energy and between the two internal energies [6]. The practical form of φ_δ and ψ_δ given here are such that the corresponding measure is invariant in the collision process. The term $(II_*/I'I'_*)^{\delta-1}$ is introduced to give the right value of

$$\gamma = \frac{\delta + 5}{\delta + 3}$$

in the limiting hydrodynamic equation of state $p = (\gamma - 1)\rho e$.

The collision cross section B measures the probability of collision of particles (v, I) and (v_*, I_*) with given parameters (ω, r, R). In the general case, it is a function of all collision invariants

$$B := B(e, R|g|, R|g \cdot \omega|, I^2 r(1-R^2), I_*^2(1-r)(1-R^2),$$
$$(1-R^2)(I^2 + I_*^2)) > 0.$$

In our simulations, we have used the classical variable hard sphere model (VHS)

$$B = C|g|^{-2\alpha}|g.\omega|R^{1-2\alpha},$$

which is the simplest model compatible with a Sutherland type viscosity law

$$\mu = KT^{1/2+\alpha}$$

at the Navier–Stokes limit. The constants C and α are optimized in order to make the Sutherland law accurate both at the wall temperature and at the stagnation temperature.

This Boltzmann equation must be complemented by boundary conditions imposing the distribution of incoming particles. In the case of perfect accommodation on the body's surface, we would have

$$\begin{aligned} f(x, v, I, t) &= \rho_\infty M_{u_\infty, T_\infty}(v, I) \quad \text{if } v \cdot n < 0 \text{ at infinity,} \\ f(x, v, I, t) &= kM_{u_w, T_w}(v, I) \quad \text{if } v \cdot n < 0 \text{ on the body's surface,} \\ \int f(x, v, I, t) v \cdot n dv dI &= 0 \quad \text{on the body's surface,} \end{aligned}$$

with $M_{u,T}$ denoting the Maxwellian distribution with mean velocity u and temperature T:

$$M_{u,T}(v, I) = \lambda_\delta \frac{\rho I^{\delta-1}}{T^{(3+\delta)/2}} e^{-(|v-u|^2+2I^2)/2T}.$$

More elaborate boundary conditions are introduced in Section 6. In any case, when the gas is dense, solving Boltzmann equation is very expensive. Hence, it is more convenient to solve Navier–Stokes equations. When the gas is nearly dense the use of Navier–Stokes model with an appropriate boundary conditions derived from the kinetic theory may give a good result (see the next paragraph for a brief discussion and [28, 7, 11] or [10], for more details on the derivation).

3. NAVIER–STOKES EQUATIONS WITH SLIP BOUNDARY CONDITIONS

The Navier–Stokes equations are given in conservative form by

$$\frac{\partial W}{\partial t} + \nabla \cdot F(W) = 0 \quad \text{on } \Omega,$$

with the state vector W and flux $F(W)$ given by

$$W = \begin{bmatrix} \rho \\ \rho u \\ \rho(e + u^2/2) \end{bmatrix}$$

$$F(W) = \begin{bmatrix} \rho u \\ \rho u \otimes u + pId - \sigma_v \\ (\rho(e + u^2/2) + p)u - \sigma_v \cdot u + q \end{bmatrix}.$$

Moreover, the internal energy e is related to the gas density ρ and pressure p by the equation of state $p = (\gamma - 1)\rho e$, the viscous stress σ_v is proportional to the deviating part of the deformation rate tensor, and the heat flux q is related to the temperature gradient by Fourier's law:

$$\begin{aligned} \sigma_v &= \mu(T)(\nabla u + \nabla^t u) - \lambda(T)\text{div } uI, \\ q &= -\lambda_T(T)\nabla T. \end{aligned}$$

Here, Ω is the physical domain, on which we impose the boundary conditions

$$W = W^\infty \quad \text{at infinity,}$$

and appropriate boundary conditions on the body as specified below.

The standard approach in rarefied regimes is to use the following slip boundary conditions on the body:

$$u \cdot n = 0, \tag{1}$$

$$\rho u \cdot \tau = K_n C_{1\beta} \partial_n (u \cdot \tau) + K_n C_{6\beta} \partial_\tau T, \tag{2}$$

$$T - T_{\text{body}} = K_n C_{2\beta} \partial_n T. \tag{3}$$

Above n denotes the unit normal vector to the wall and τ any tangential direction.

Such boundary conditions can be obtained as in Gupta, Moss, and Scott [11] by assuming that half-flux are conserved in the kinetic boundary layer. Alternatively, for monoatomic gases, these boundary conditions are obtained in Coron [10] by solving the Boltzman equation at order (K_n^2), approximating f by the asymptotic equation

$$\begin{aligned} F_\varepsilon(x, v, t) &= M_{u,T}(v)[\rho - K_n \phi(x, v, t)] \\ &\quad + \chi\left(\frac{d(x, \text{body})}{K_n}, v, t\right) + K_n^2 C(x, v, t), \\ K_n \phi(x, v, t) &= \frac{2}{5} \frac{\lambda}{\rho(rT)^2} \left(\frac{(v-u)^2}{2rT} - \frac{5}{2}\right)(v-u) \cdot \text{grad } T \\ &\quad - \frac{\mu}{\rho(rT)^2} \Big((v-u) \otimes (v-u) \\ &\quad - \frac{1}{3}(v-u)^2 \text{Id} \Big) : \text{grad } u. \end{aligned}$$

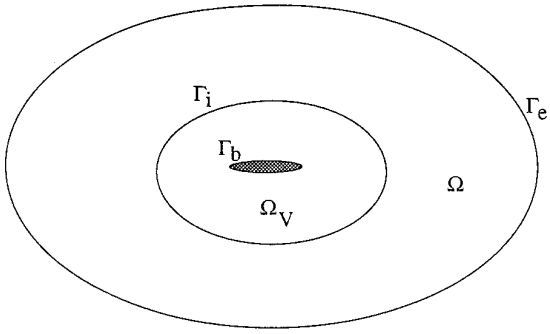

FIG. 2. The global geometry.

Above, $M_{u,T}(v)$ is the standard Maxwellian distribution, ϕ is the Chapman–Enskog correction used in the derivation of the Navier–Stokes equation [10], and χ is a boundary layer correcting term.

The boundary conditions (2) and (3) involve constants $C_{i\beta}$ which are hard to identify and their derivation uses a priori assumptions which turn out to be quite arbitrary. Moreover, their extension to diatomic gases is quite delicate. Hence we would like to replace them by flux boundary conditions of the type

$$\sigma_v \cdot \tau = g_1,$$
$$-q \cdot n + u_\tau \cdot \sigma_v \cdot n = g_2,$$

where the friction stress vector g_1 and energy flux g_2 would be computed numerically by a local kinetic model.

The proposed method is, therefore, to couple these Navier–Stokes equations to the Boltzmann equation, where Navier–Stokes equations are used everywhere on the domain, except at the obstacle and the Boltzmann equation is used in a small domain surrounding the obstacle. The friction fluxes are then obtained from the Boltzmann equations and plugged as wall boundary conditions in the global Navier–Stokes system.

4. BOLTZMANN/NAVIER–STOKES COUPLING

4.1. *Coupled Problem*

Let us consider the geometry described in Fig. 2. Let $f(x, v, I, t)$ denotes the particle distribution in the Boltzmann region Ω_V, which is a small region surrounding the body. Let $W = (\rho, \rho u, \rho(e + u^2/2))$ be the value of the conservative variable as computed by a Navier–Stokes model in the whole domain Ω. On Ω_V, we solve the Boltzmann equation

$$\frac{\partial f}{\partial t} + v \frac{\partial f}{\partial x} = Q(f, f),$$

with boundary conditions

$$f(v)|_s = \rho M_{u,T}(v, I) \quad \text{if } v \cdot n < 0,$$
$$f(v)|_{\text{body}} = k M_{u_{w,T_w}}(v, I) \quad \text{if } v \cdot n < 0.$$

Everywhere in Ω, we solve the Navier–Stokes equations

$$\frac{\partial W}{\partial t} + \operatorname{div} F(W) = 0,$$

with flux boundary conditions

$$W = W^\infty \quad \text{at infinity,}$$
$$F(W) \cdot n = \begin{bmatrix} 0 \\ n \cdot \sigma(W) \cdot n \\ \tau \cdot \sigma_{\text{Bol}} \cdot n \\ -q_{\text{Bol}} \cdot n \end{bmatrix} \quad \text{on the body.}$$

Here, $\tau \cdot \sigma_{\text{Bol}} \cdot n$ and $q_{\text{Bol}} \cdot n$ are the total friction fluxes predicted and computed by the Boltzmann model. The coupling from Boltzmann to Navier–Stokes is therefore achieved by imposing these wall fluxes. Conversely, the Navier–Stokes model acts on the Boltzmann solution by imposing the incoming velocity distribution $\rho M_{u,T}(v)$ on the interface S, where (ρ, u, T) are the density, velocity, and temperature locally predicted by the Navier–Stokes model. As advocated in [17], to be more accurate, one should equal the incoming Boltzmann distribution to the modified Chapman expansion $\rho M_{u,T}[1 - (1/2\rho)K_m\phi]^2$. In all our numerical tests, we have worked in rather dense regimes with rather thick Boltzmann regions, and then the correction $[1 - (1/2\rho)K_n\phi]^2$ appears to have little effect.

4.2. *Consistency*

Since the Boltzmann equation behaves in space like a first-order transport equation, imposing the velocity distribution of the incoming particles completely defines the Boltzmann solution inside Ω_V. Similarly, the above boundary conditions on W define a well-posed Navier–Stokes problem [25], Chap. 6; [27]. Indeed, in such a problem, we can impose either a zero normal mass flux or a normal stress, either a tangential velocity or a tangential stress, and either a given temperature or a given energy flux. The combination of imposed zero mass flux, tangential stress, and heat flux is thus perfectly appropriate.

Without changing the global Navier–Stokes solver, it gives an easy way of supplementing and testing a large variety of kinetic boundary conditions. These kinetic boundary conditions are first imposed on the Boltzmann model, and the resulting fluxes σ_{Bol} and q_{Bol} are then

plugged in the Navier–Stokes equations. They correspond to the losses in tangential momentum and energy of particles colliding into the wall.

4.3. *Interpretation*

The interpretation of the above coupled strategy is easy when coupling the same equation on overlapping domains. If we make additional assumption, similar argument, as has been seen in [25, 26] for Navier–Stokes/Navier–Stokes coupling can still hold for the Boltzmann/Navier–Stokes coupling.

In particular, we can justify our coupling strategy provided that we assume that imposing friction forces on Γ_b, given inflow data on Γ_∞ and using either Boltzmann equations or Navier–Stokes equations on Ω lead to the same kinetic physical solution f_{glo} outside Ω_V. (For the Boltzmann model, we would supplement the friction forces by an additional information extracted from f_{loc} in order to get a well posed global problem). Then f_{loc} and f_{glo} would satisfy:

equality of velocity distribution on the interfaces,

equality of friction forces (+ additional information) on the wall Γ_b,

the same Boltzmann equation on Ω_V.

We would deduce as for the Navier–Stokes/Navier–Stokes coupling [25, 26] that the two distributions f_{loc} and f_{glo} are equal inside the local domain and in particular at the wall. Then, f_{glo} satisfying the kinetic conditions imposed to f_{loc} on the wall, the Boltzmann equation on Ω, and the adequate inflow boundary conditions on Γ_∞ is the desired Boltzmann solution. In turn, this means that f_{loc} is locally equal to the desired solution. Therefore, if our assumption is true, f_{loc} is locally the kinetic solution which has been computed at low cost by using a coarse-averaged Navier–Stokes approximation away from the wall (outside Ω_V).

4.4. *Algorithm*

The numerical solution of this coupled model can be easily achieved by the following algorithm:

Initialization

Solve Navier–Stokes equations on the whole domain (using a coarse mesh, a conservative formulation, flux splitting and, say, slip boundary conditions).

Loop on time: For increasing time n and until reaching a steady state,

1. Solve several time steps of the local Boltzmann solver

$$(f_{n+1} - f_n)/DT + v \cdot \nabla f_n = Q(f_n, f_n),$$
$$f^-_{n+1} = M_{u,T}(v)(\rho - K_n \phi) \quad \text{on the interface } S,$$
$$f^-_{n+1} = k M_{u_{w,T_w}}(v) \quad \text{on the body.}$$

2. From f_{n+1} compute the friction fluxes $F_b = (\tau \cdot \sigma_{\text{Bol}} \cdot n, -q_{\text{Bol}} \cdot n)$ on the body.
3. With imposed friction fluxes F_b, solve several time steps of the global Navier–Stokes equations

$$(W^g_{n+1} - W^g_n)/DT + F_{i,i}(W^g_{n+1}) = 0,$$
$$F(W^g_{n+1}) \cdot n = (0, n \cdot \sigma(W^g_{n+1}) \cdot n, F_b) \quad \text{on the internal boundary } \Gamma_b$$

and with the usual boundary conditions at infinity.

The whole strategy has been proposed in the phase research and development of the Hermes program (see [25]). At that time it was tested with a frozen viscosity in the Navier–Stokes domain and with a monoatomic hard sphere model in the Boltzmann region. More sophisticated models will be introduced here. This includes variable viscosity for the Navier–Stokes solver, the variable hard sphere model, and the Larsen–Borgnakke model for the Boltzmann solver [4]. These enhanced models are then validated on several configurations as will be seen in the next sections.

Remark 4.1. Compared with the flux matching strategies of [3, 16] or with the coupling strategy of [17] which both use very little overlapping between the kinetic and the hydrodynamic region, the coupling by friction described herein is:

—simpler because the Navier–Stokes solver is used on the whole physical domain,
—less sensitive to the choice of interface S (we do not need to match isolines at this interface), which makes it more robust at dense regimes,
—but restricted to rather dense situations because it integrates the Navier–Stokes model up to the wall.

By contrast, the coupled approach of [17] was mainly used for rather rarefied regimes, and faces difficulties for denser cases.

5. NAVIER–STOKES SOLVER

Let us consider the compressible Navier–Stokes equations which we formally write as

$$\frac{\partial W}{\partial t} + \text{div}[F(W)] = 0 \quad \text{on } \Omega, \tag{4}$$

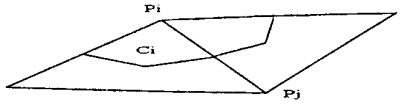

FIG. 3. A boundary cell.

with $W = (\rho, \rho u, \rho(e + u^2/2))$ the conservative variables, and $F = F^c + F^d$ the total flux (convective and viscous part). The problem consists in computing a steady solution of these equations, satisfying the boundary conditions introduced in the previous section

$$W = W^\infty \quad \text{at infinity,}$$

$$F(W)\cdot n = \begin{bmatrix} 0 \\ n\cdot\sigma(W)\cdot n \\ \tau\cdot\sigma_{\text{Bol}}\cdot n \\ -q_{\text{Bol}}\cdot n \end{bmatrix} \quad \text{on the body.}$$

The global domain Ω is discretized using node centered cells (Fig. 3) defined on an unstructured grid. Then, at each time step n and for each cell i, we solve

$$\int_{C_i}\frac{W^{n+1}-W^n}{\Delta t} + \sum_{j\in V(i)}\int_{\partial C_i\cap\partial C_j} F^c(W^n)\cdot n_i + \int_\Omega F^d(W^n)\cdot\nabla\varphi_i + \int_{\partial C_i\cap\Gamma_\infty} F(W^n)\cdot n_i = -\int_{\partial C_i\cap\Gamma_b} F\cdot n_i.$$

Above φ_i is the nodal shape function associated to the node i, that is, the continuous piecewise linear function with value 1 at node i and 0 at all other nodes.

In all present numerical tests, in order to be robust in hypersonic regimes and to always return positive pressures and densities, we compute the convective flux

$$\int_{\partial C_i\cap\partial C_j} F^c(W^{n+1})\cdot n_i$$

by the hybrid upwind splitting (HUS) scheme of [9]. This scheme corrects the flux vector splitting of [20] by the formula

$$\begin{aligned} F(W_i,W_j) &= F^+(W_i) + F^-(W_j) - F^-(W_{\text{R}}^*) \\ &\quad + F^-(W_{\text{L}}^*) \quad \text{if } v^* \geq 0 \\ &= F^+(W_i) + F^-(W_j) + F^+(W_{\text{R}}^*) \\ &\quad - F^+(W_{\text{L}}^*) \quad \text{if not.} \end{aligned}$$

Above W_{R}^* and W_{L}^* are the left and right states calculated in the Osher–Solomon approximate Riemann solver (used in reverse order) and v^* is the speed of the contact discontinuity separating W_{R}^* and W_{L}^*.

By construction, this scheme returns positive pressures and densities, which makes it very robust in hypersonic situations. It also treats exactly contact discontinuities and therefore is less diffusive than the underlying kinetic scheme. Its second-order implementation was realized by first computing nodal averages of gradients of W, and then constructing second-order approximations W_{ij} and W_{ji} at $\partial C_i \cap \partial C_j$ using a MUSCL scheme with Van Albada limiters. In order to preserve its robustness, the scheme is automatically degraded to first order as soon as a minmod indicator detects gradient inversions.

On the body Γ_b, because of our special choice of boundary conditions, the flux is given by

$$\int_{\partial C_i\cap\Gamma_b} F\cdot n_i = \int_{\partial C_i\cap\Gamma_b}\begin{pmatrix} 0 \\ n_i\cdot\sigma(W^n)\cdot n_i \\ n_i\cdot\sigma_{\text{Bol}}\cdot\tau_i \\ -q_{\text{Bol}}\cdot n_i \end{pmatrix}. \tag{5}$$

Remark 5.1. Imposing friction forces to the global solution instead of no slip boundary conditions allows us to have an accurate solution away from the boundary layer even with a coarse mesh (see [25]).

6. BOLTZMANN SOLVER

In this section, we will present first the numerical approximation methods used to solve the Boltzmann equation. Then we describe the treatment of the boundary conditions and the calculation of momentum and energy fluxes on the body.

6.1. *Approximation of the Boltzmann Equation*

We have chosen to solve the Boltzmann equation by the particle method proposed by Babovski [2] and described in [5, 19]. The main ingredient is to decouple at each time step the transport phase from the collision phase.

The free transport phase solves

$$\frac{\partial f}{\partial t} + v\nabla_x f = 0, \quad f(t_n) = f_n, \tag{6}$$

the collision phase solves

$$\frac{\partial f}{\partial t} - Q(f,f) = 0, \quad f(t_n) = f_{n+1}^{\text{transport}}. \tag{7}$$

These two steps are realized successively. For this purpose, particle approximations of kinetic equations are introduced, based on the approximation of the density f by a sum of Dirac mass

$$f(t,x,v,I) = \frac{1}{n_\infty}\sum_{i=1}^{N} \delta(x - x_i(t))\delta((v,I) - (v_i,I_i)(t)). \tag{8}$$

The positions $x_i(t)$ change during the free transport phase only and are updated following (6) by

$$x_i(t + \Delta t) = x_i(t) + \Delta t v_i(t).$$

The velocities and internal energies $(v_i(t), I_i(t))$ change during the collision step (7). At this step, one covers the computational domain with regular cells C_i, and one solves the collision step separately on each cell, taking as initial distribution

$$f(v, t=0)_{|C_j} = \frac{1}{n_\infty}\sum_{i\in C_j} \delta((v,I) - (v_i,I_i)(0)).$$

Following [2], we solve (7) under the weak form

$$\begin{aligned}\frac{d}{dt}\langle f(t), g\rangle &= \langle Q(f,f), g\rangle \\ &= \frac{1}{2}\int ff_*(g' + g'_*)Bdm \\ &\quad - \frac{1}{2}\int ff_*(g + g_*)Bdm,\end{aligned} \tag{9}$$

where g is any continuous function and where we have used the notation

$$\langle f, g\rangle = \int_{\mathbb{R}^3\times\mathbb{R}_+} f(v,I)g(v,I)dvdI,$$

$$dm = dvdv_*dIdI_*\varphi_\delta\psi_\delta drdRd\omega.$$

The above writing of the collision operator is a consequence of the microreversibility of each individual collision and stays valid even if f is a sum of Dirac distributions. For our choice of f, the scattering term is then simply

$$\frac{1}{2}\int ff_*(g + g_*)Bdm = \frac{1}{2n_\infty^2}\sum_{i\neq j}[g(v_i,I_i) + g(v_j,I_j)]W_{v_i,v_j}, \tag{10}$$

with weight W_{v_i,v_j} given by

$$W_{v_i,v_j} = \int B\varphi_\delta\psi_\delta drdRd\omega.$$

The source term in (9) is similarly

$$\frac{1}{2}\int ff_*(g' + g'_*)Bdm = \frac{1}{2n_\infty^2}\sum_{i\neq j}\int [g(v_i', I_i') + g(v_j', I_j')]B\varphi_\delta\psi_\delta drdRd\omega, \tag{11}$$

with v_i', v_j', I_i', I_j' the result of the collision of (v_i, I_i) with (v_j, I_j).

We then integrate (7) in time by:

• replacing the double sum in (10) or (11) by $(N-1)$ times the sum carried over a random choice of $N/2$ pairs of particles

$$\sigma = \{(v_1,I_1),(v_{*1},I_{*1})\},\{(v_2,I_2),(v_{*2},I_{*2})\},\ldots,\{(v_{N/2},I_{N/2}),(v_{*N/2},I_{*N/2})\};$$

• discretizing (7) in time by the explicit Euler scheme

$$\begin{aligned}\langle f^{n+1}, g\rangle &= \langle f^n, g\rangle + \Delta t[\text{source-scattering}] \\ &= \frac{1}{n_\infty}\sum_{i=1}^{N/2}[g(v_i,I_i) + g(v_{*i},I_{*i})]\left(1 - \frac{N-1}{n_\infty}\Delta t W_{v_i,v_{*i}}\right) \\ &\quad + \frac{N-1}{n_\infty}\Delta t\int [g(v_i',I_i') + g(v_{*i}',I_{*i}')]B_i\varphi_\delta\psi_\delta drdRd\omega;\end{aligned}$$

• using the identities (assume that $\varphi_\delta(r)\psi_\delta(R)drdRd\omega$ is normalized so as to be a probability measure)

$$\frac{N-1}{n_\infty}\Delta t B_i = \int \mathbf{1}_{0\le s\le (N-1)/n_\infty B_i\Delta t} ds,$$

$$1 - \frac{N-1}{n_\infty}\Delta t W_{v_i,v_{*i}} = \int\int \mathbf{1}_{(N-1)/n_\infty B_i\Delta t\le s\le 1}\, ds\varphi_\delta\psi_\delta drdRd\omega;$$

• and computing all integrals using a Monte-Carlo method.

In practice, once the random choice of the $N/2$ pairs has been made, we perform for each pair a random choice of r, R, ω according to the law $\varphi_\delta\psi_\delta drdRd\omega$, and a uniformly random choice of $s_i \in (0,1)$. Then, if $s_i \le ((N-1)/n_\infty)\,\Delta t B_i$, the source term $1 - ((N-1)/n_\infty)\,\Delta t W_{v_i,v_{*i}}$ is zero, the scattering term $((N-1)/n_\infty)\,\Delta t B_i$ is equal to one, and

thus the collision is processed: the particles $(v, I)_i, (v_*, I_*)_i$ are replaced by the particles $(v', I')_i, (v'_*, I'_*)_i$ obtained in the collision with parameters r, R, ω. If not, the pair of particles is kept unchanged. The final distribution is then

$$\begin{aligned} f^{n+1} = \frac{1}{n_\infty} \sum_{i \in I_1} & \{\delta((v, I) - (v_i, I_i)) \\ & + \delta((v, I) - (v_{*i}, I_{*i}))\} \\ & \times \sum_{i \notin I_1} \{\delta((v, I) - (v'_i, I'_i)) \\ & + \delta((v, I) - (v'_{*i}, I'_{*i}))\}, \end{aligned}$$

where I_1 denotes the set

$$I_1 = \left\{ i, 1 \le i \le N/2, s_i > \frac{N-1}{n_\infty} \Delta t B_i \right\}.$$

The complexity of this algorithm is in $O(N)$. Moreover, by construction, this algorithm conserves exactly mass, momentum, and energy.

6.2. *Numerical Algorithm*

The numerical algorithm corresponds to the Monte-Carlo method described above and was initially developed at the University of Kaiserslautern. This algorithm is the following:

1. Get an initial distribution of particles.
2. Loop in time from 1 to N_2:

• generate randomly the particles at the external boundary;

• advance the particles in free transport

$$x_i(t + \Delta t) = x_i + v_i \Delta t;$$

• erase the particles that leave the domain, except those which get in contact with the obstacle and which are reflected as indicated later;

• accomplish the intermolecular collision as indicated above.

As output, the average values, ρ, u, T and the fluxes at the body are obtained by averaging the corresponding kinetic quantities over all particles of the cell considered and on several ($\ge$100) consecutive time steps. The fluxes at the body (friction forces and heat fluxes) are calculated using their kinetic definitions. Under the notation

n, external unit normal to the physical domain;

Γ, surface section on which we integrate the flux;

dS, area of Γ;

dt, time interval considered;

the quantity $\sigma \cdot ndSdt$ corresponds to the impulse exerted on the fluid by the surface section Γ during the time interval dt, i.e., to the sum of impulses received by the elementary particles which collide with Γ during the time interval dt, and v_i^-, v_i^+ the velocities of the colliding particle before and after its impact on the wall. We then have

$$\sigma_{\text{Bol}} \cdot ndSdt = \sum_{i \in J} m_i (v_i^+ - v_i^-),$$

with J denoting the set of particles which collide with Γ during the time interval dt. Therefore, we have the final formula,

$$\sigma_{\text{Bol}} \cdot n = \frac{\rho^\infty \text{vol}^\infty}{n^\infty dSdt} \sum_{i \in J} (v_i^+ - v_i^-)$$

with ρ^∞, vol^∞, and n^∞ denoting respectively the density, volume, and number of particles associated with a reference cell of the flow at infinity. Similarly $q_{\text{Bol}} \cdot ndSdt = (n \cdot \sigma \cdot u - q \cdot n) dSdt$ is the energy received by the fluid on the section Γ during the time interval dt, which gives

$$q_{\text{Bol}} \cdot ndSdt = -\sum_{i \in J} (\tfrac{1}{2} m_i |v_i^+|^2 + I_i^+ - \tfrac{1}{2} m_i |v_i^-|^2 - I_i^-).$$

Remark 6.1. In order to minimize the memory place, at each call to the local Boltzmann solver, we initialize the initial distribution of the particles by the Maxwellians M_i defined at each cell i and whose parameters ρ_i, u_i, and T_i are either the average values ρ_i^{N-1}, u_i^{N-1}, and T_i^{N-1} computed at the previous call to the Boltzmann solver, or the values given by the present Navier–Stokes solution.

6.3. *Boundary Conditions at Infinity*

In classical situations, the boundary conditions at infinity consist in imposing the distribution of the ingoing particles equal to the Maxwellian at infinity. We mean by infinity that the limit of the domain is fixed far away from the obstacle.

Herein, we want to solve a local Boltzmann problem in a small domain surrounding the obstacle. In this domain, the external boundary conditions are computed from the global Navier–Stokes solver. To adapt these new boundary conditions (instead of the classical boundary conditions at infinity) to these particular geometries, we introduce an external layer of boundary cells. We compute at the center of each cell the quantities ρ, u, and T predicted by the current Navier–Stokes calculation. To do so, we look for the triangle in the global mesh which contains the center i of the boundary cell and we compute ρ_i, u_i, and T_i by linear interpolation. Then, we introduce in this cell ($\rho_i N^\infty$) particles. These particles are distributed randomly in space,

and their velocities and energies are obtained by drawing them randomly according to the Maxwellian distribution $M(u_i, T_i)$.

These particles are finally transported by their velocity field and we take into account only the particles which enter effectively the local domain during the time step considered. This operation is repeated at each time step of the local Boltzmann solver.

To be perfectly accurate, as indicated earlier, we should replace the Maxwellian distribution $M(u_i, T_i)$ by an approximation of the Chapman–Enskog expansion $M(u_i, T_i)(\rho - K_n\phi)$, but this seems to have very little effect on the global solution.

6.4. *Boundary Conditions on the Body*

In kinetic theory, the interaction between the gas and the body is expressed by a boundary condition acting on the density distribution $f(x, v, t)$. These interactions on the body are very complex and very hard to model. Therefore we restrict ourselves to the total accommodation model of Section 2. In certain specific tests, we have also used the intermediate Maxwell accommodation model given by

$$f(x, \xi, I) = \beta(x) f(x, R\xi, I) + (1 - \beta(x))\alpha(x) M_{0,T}(\xi, I)$$

$$\forall \xi \text{ such that } \xi \cdot n > 0,$$

$$\forall x \in \partial\Omega, \quad \int \xi \cdot n(x) f(x, \xi, I) d\xi dI = 0.$$

Above, $n(x)$ is the external normal to the obstacle at $x \in \partial\Omega$, $\beta(x) \in (0, 1)$ is the Maxwell accommodation coefficient and

$$R\xi = \xi - 2(\xi \cdot n(x))n(x)$$

is the velocity of the particle after elastic reflexion on the obstacle.

This boundary condition is imposed numerically to all particles which collide into the obstacle during their free transport. These are reflected after impact with velocity v^+ and internal energy I^+ given by total accommodation $(v^+ = v_a^+, I^+ = I_a^+)$ if $a < \beta$, and by specular reflexion if not. Above, the coefficient a is a random number uniformly chosen in the interval (0, 1), and (v_a^+, I_a^+) is calculated by randomly drawing (v, I) following the probability distribution $\lambda M_{0,T}(\xi, I)$.

7. NUMERICAL RESULTS

7.1. *Sensitivity to the Choice of the Local Domain and to the Downstream Boundary Conditions*

This monoatomic test case corresponds to a flow above a flat plate at no angle of attack with

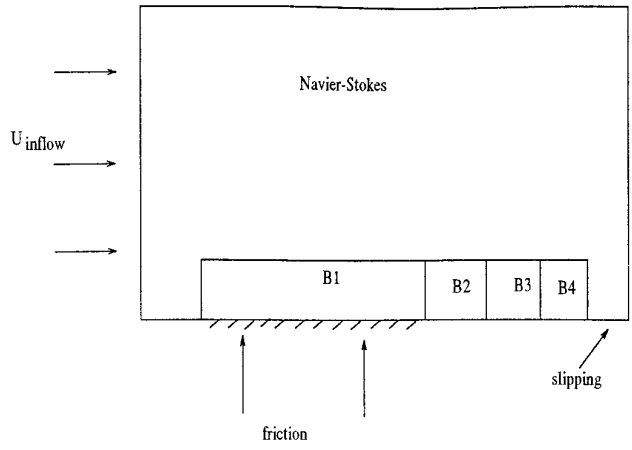

FIG. 4. Coupling geometry with different local subdomains.

M_∞	Re_∞/m	T_∞	T_{wall}
10.	143.800	52 K	290 K

We compare in this paragraph the results obtained when considering a local Boltzmann domain that is smaller and smaller. More precisely, the plate takes respectively the length of 11 cm (L1), 10 cm (L2), 7 cm (L3), and 5 cm (L4) (see Fig. 4). The local length in the vertical projection is 1 cm and does not change for all configurations described above.

For all these calculations, the size of the cells in x and y direction is almost the same for the local calculation. The sensitivity to the choice of the local domain is studied on the friction coefficient C_f, the heat flux coefficient C_A, the slip velocities, and the normal stress vector. The viscosity law considered here is the VHS law $\mu = CT^w$ with $w = 0.93$ and $C = 6.9\ 10^{-6}$ SI.

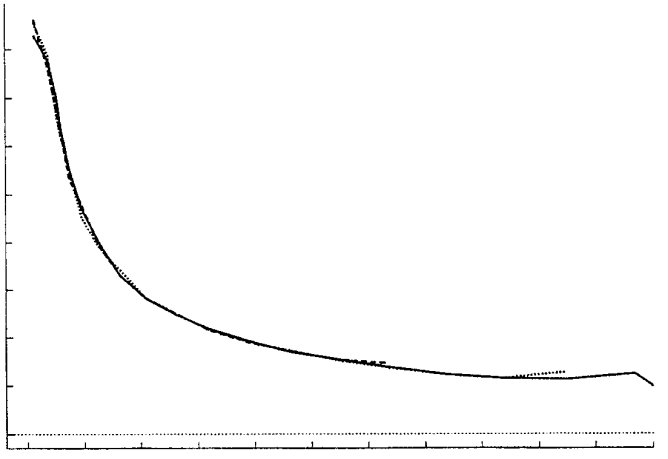

FIG. 5. Values of C_f for different subdomain sizes. Values range from 0.08 to 0.02 and all curves are perfectly superposed.

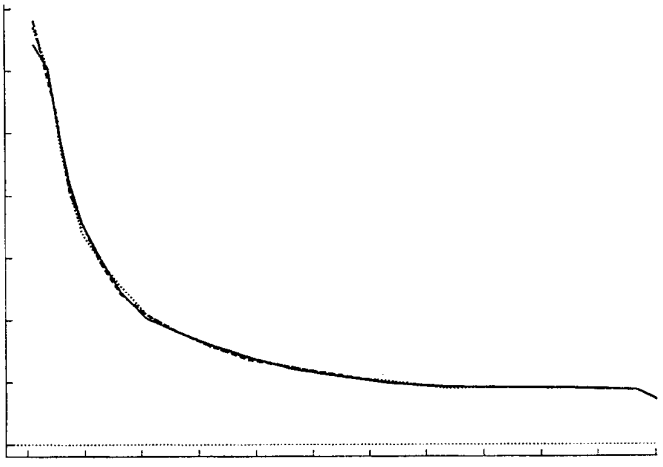

FIG. 6. Values of C_h for different subdomain sizes. Values range from 0.035 to 0.005 and all curves are perfectly superposed.

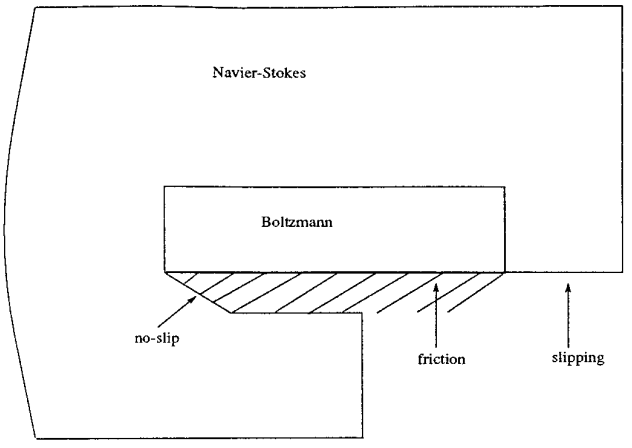

FIG. 7. Plate problem.

We present on Fig. 5 the C_f corresponding to the calculations $L1$, $L2$, $L3$, and $L4$. We observe that the curves obtained are perfectly identical. The heat flux corresponding to the calculation $L1$, $L2$, $L3$, and $L4$ are presented in Fig. 6. The results obtained are also perfectly identical.

In conclusion, the choice of the local domain corresponding to the calculation $L4$ is sufficient. The boundary conditions imposed on the downstream part of the plate in the global domain are satisfactory and do not affect the solution upstream.

Remark 7.1. The number of cells in the Boltzmann calculation is 3350, the number of the Boltzmann particles is 83750, the total number of time steps for Boltzmann is 1300, the total number of time steps for Navier–Stokes is 608, the number of coupling algorithm iterations is 5.

7.2. *Study of ONERA Test Case without Angle of Attack*

The case studied here corresponds to the geometry given on Fig. 7 (10-cm long flat plate at no angle of attack) and to the following data:

Mach number = 20,

Temperature at infinity $T_\infty(K) = 13.6$,

Temperature at the body $T_W(K) = 286$,

Vitesse $V_\infty(m/s) = 1502$,

Mean free path $\lambda_\infty(m) = 5.4\ 10^{-4}$ (Knudsen = 510^{-3}),

Reynolds number per meter = 44500,

Dimensions of the Boltzmann domain $L(m) = 0.105$, $H(m) = 0.04$,

Exponent of the viscosity law $w = 0.75$,

The constant of the viscosity law $C = 2.48 \times 10^{-7}$.

This case has been studied by using our coupling strategy and is compared to the results of a full kinetic simulation and to experimental results [12, 1].

The full Boltzmann simulation uses a diatomic gas, 310000 particles, 17000-cells, 2900 time steps, the time averages being performed on the last 2000 time steps. The total CPU time was of 8 h on a HP9000/L735 workstation. Considerable care was taken in the choice of the viscosity coefficients. The values of constants C and ω used here are based on a viscosity fit for a temperature range of 200 to 500 K. This updated choice of viscosity coefficients gives a much better agreement with the available experimental results.

In the coupled simulation, run on two iterations, the local Boltzmann domain is four times thinner (Fig. 9), but uses twice as much cells. The total CPU time of the local Boltzmann solver is 1 h, with an average of 70000 particles. The Navier–Stokes mesh of the coupled simulation is presented on Fig. 8 and contains 3600 vertices. The Navier–Stokes solver was not optimized and used a total of 10000 explicit time steps for a CPU time of 3 h. Coupling was

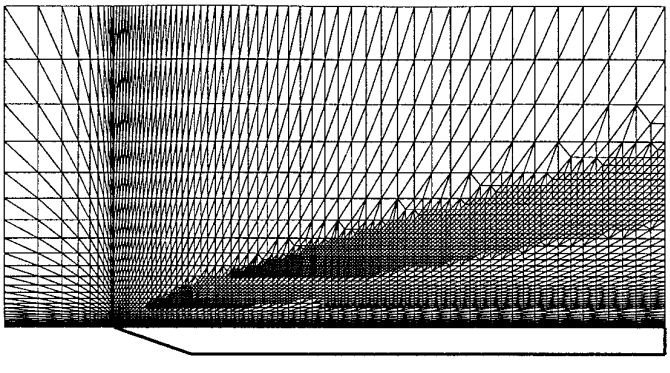

FIG. 8. Plate problem: Mesh used for the coupled Navier–Stokes model.

FIG. 9. Plate problem: Zoom on the isodensity lines predicted by the local Boltzmann solver on the local Boltzmann domain.

realized through a Unix shell script iteratively calling the Boltzmann code and the Navier–Stokes solver.

The first curves compare density profiles at the tip of the plate (Fig. 10) and temperature profiles further down (Fig. 11) as predicted by the global Boltzmann solver or by the local coupled Boltzmann solver. The agreement is perfect.

The next set of figures (Figs. 12, 13) represent wall and heat friction coefficients as computed in the global Boltzmann model, the local Boltzmann coupled model, the local Navier–Stokes coupled model and a global Navier–Stokes model with linear slip boundary conditions. The coupled values (either Boltzmann, or Navier–Stokes) are in perfect agreement with the global value, and differ substantially from the global Navier–Stokes solution. The expected concordance between both coupled solutions at the wall confirms that the weak imposition of the kinetic friction fluxes is correctly taken into account by the Navier–Stokes solver.

The situation is slightly different on density and temperature profiles. On Figs. 14, 15, and 16, we have compared experimental results (only available for density profiles) with the kinetic results (either global or local coupled which are identical on their common domain of definition), the coupled Navier–Stokes profiles and the global Navier–Stokes profiles (computed with linear slip boundary conditions). Kinetic results are in quite good agreement with the experimental results when available, but do not correspond to the Navier–Stokes profiles. In particular, temperature and velocity jumps predicted at the wall by the kinetic

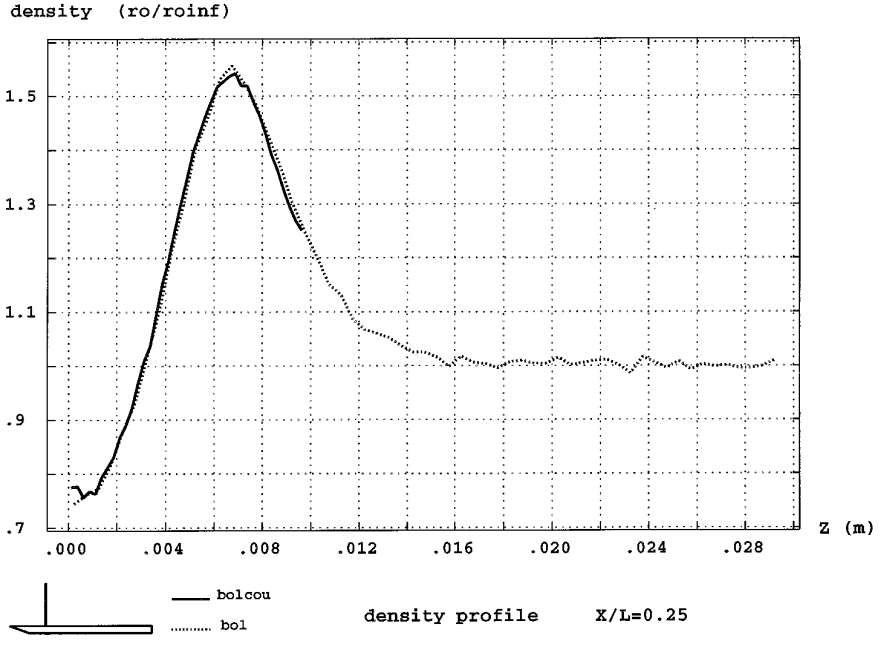

FIG. 10. Plate problem: Density profiles predicted by the global Boltzmann solver and by the local coupled Boltzmann solver.

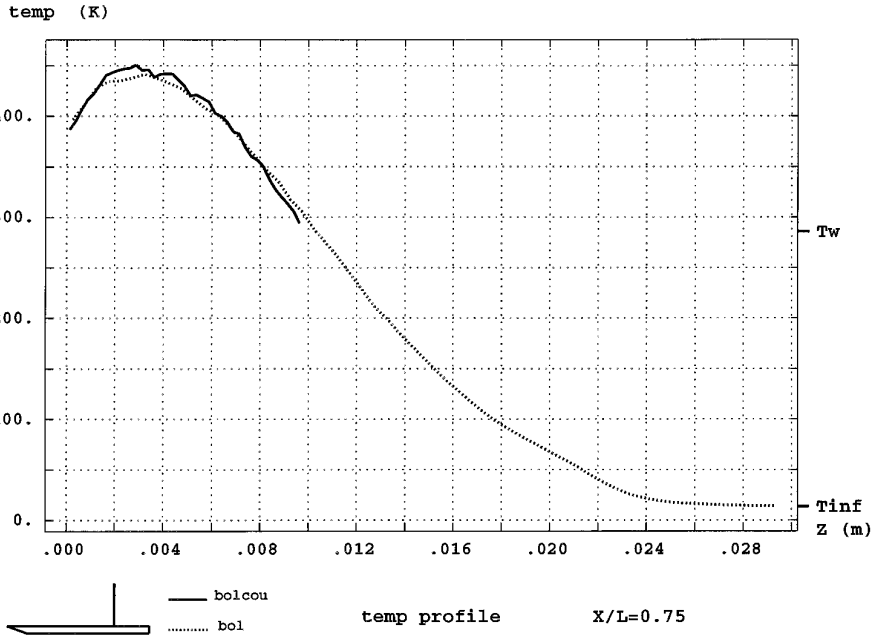

FIG. 11. Plate problem: Temperature profiles predicted by the global Boltzmann solver and by the local coupled Boltzmann solver.

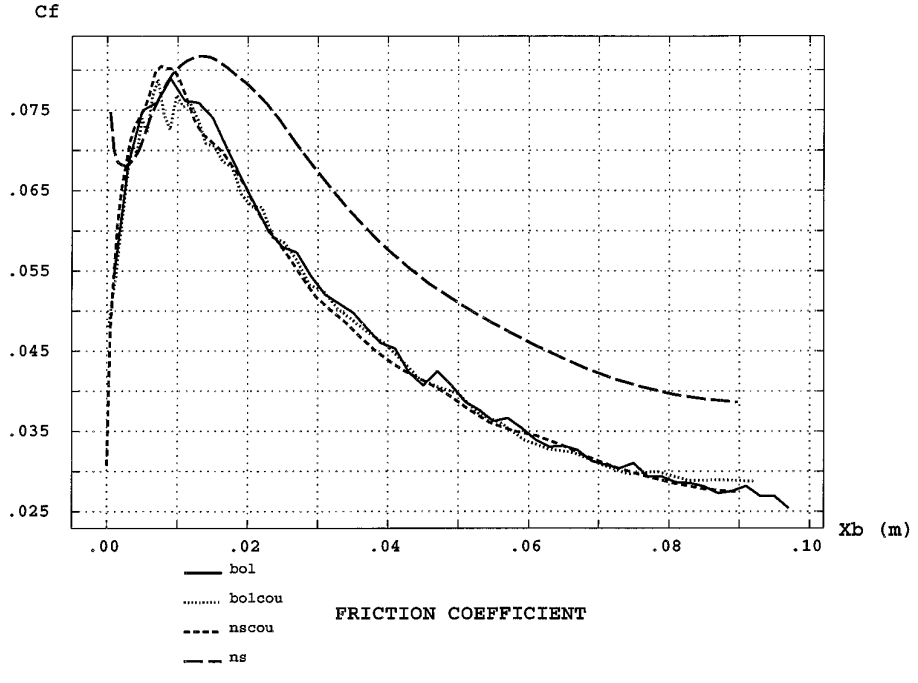

FIG. 12. Plate problem: Wall friction coefficients predicted by the global Boltzmann solver, by the local coupled Boltzmann solver, by the coupled Navier–Stokes solver and by a global Navier–Stokes solver with linear slip boundary conditions. The prediction of the Navier–Stokes solver with linear slip boundary conditions differs significantly from the kinetic predictions.

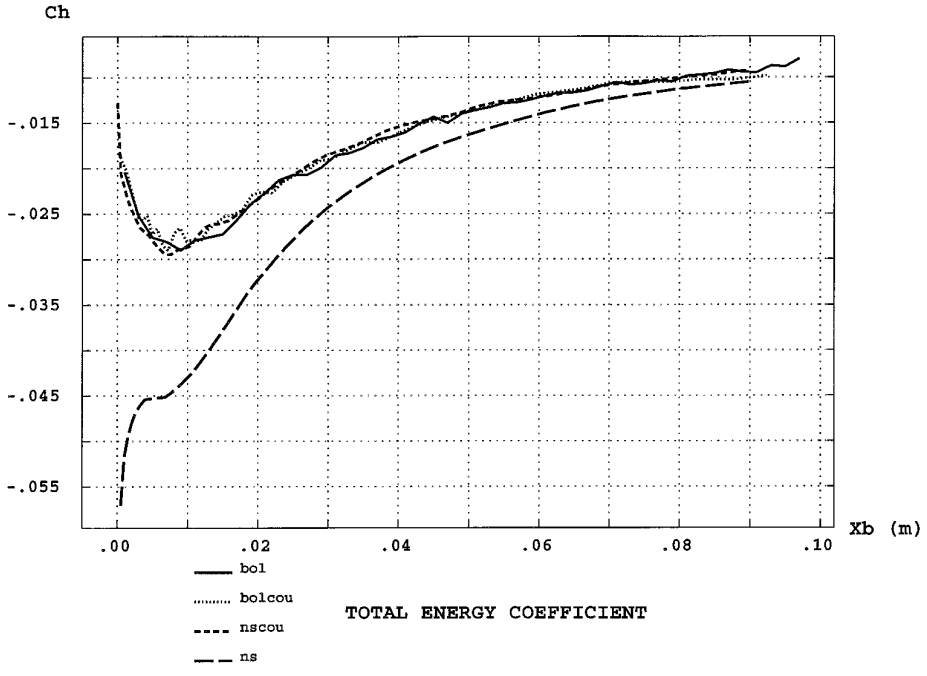

FIG. 13. Plate problem: Wall heat coefficients predicted by the global Boltzmann solver, by the local coupled Boltzmann solver, by the coupled Navier–Stokes solver and by a global Navier–Stokes solver with linear slip boundary conditions.

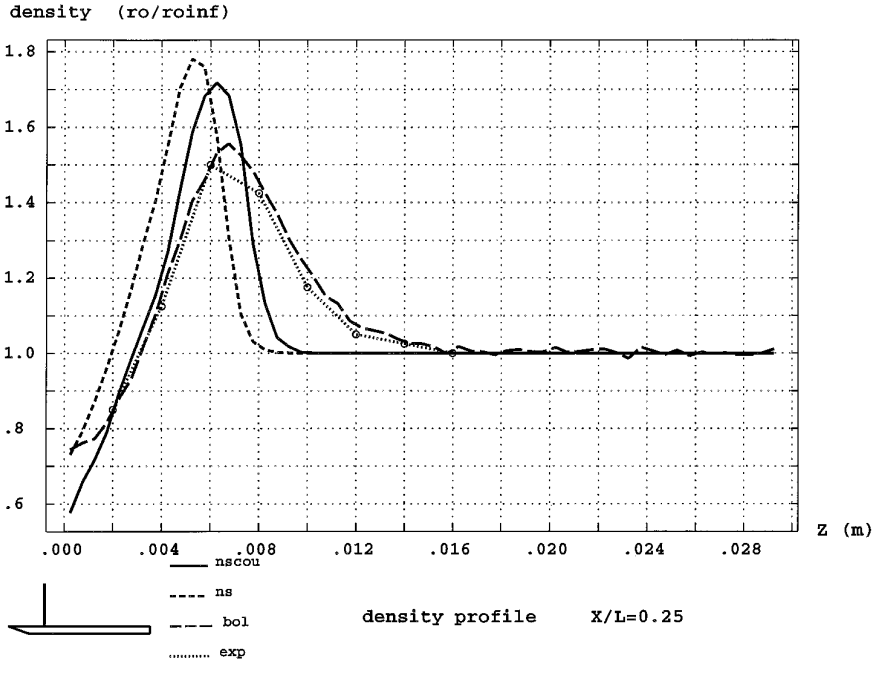

FIG. 14. Plate problem: Experimental density profiles at the tip of the plate as compared to those predicted by the global Boltzmann solver, by the coupled Navier–Stokes solver and by a global Navier–Stokes solver with linear slip boundary conditions. The kinetic prediction is quite reasonable but differs from the Navier–Stokes profiles of either the coupled approach or the global approach.

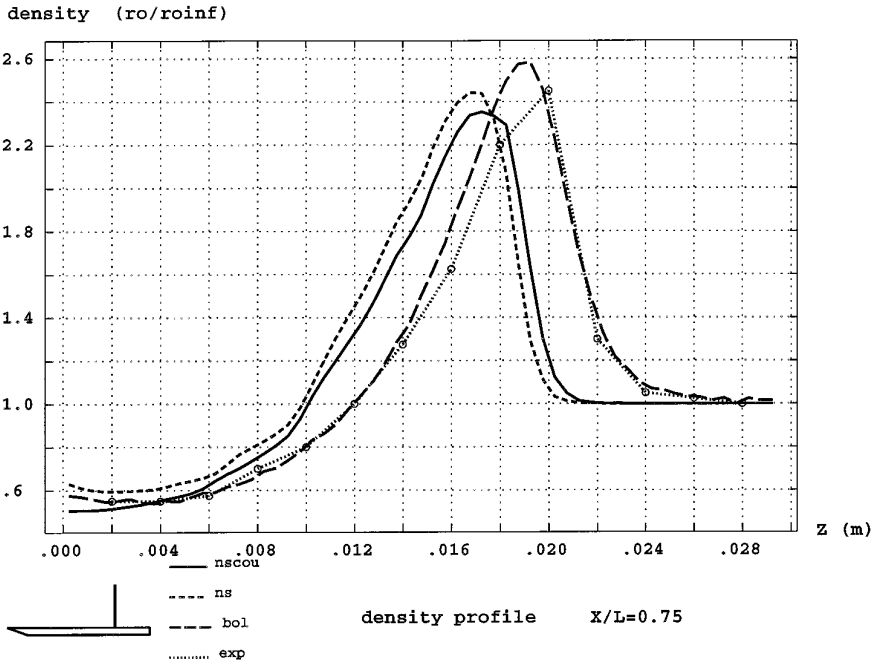

FIG. 15. Plate problem: Experimental density profiles down the plate as compared to those predicted by the global Boltzmann solver, by the coupled Navier–Stokes solver and by a global Navier–Stokes solver with linear slip boundary conditions.

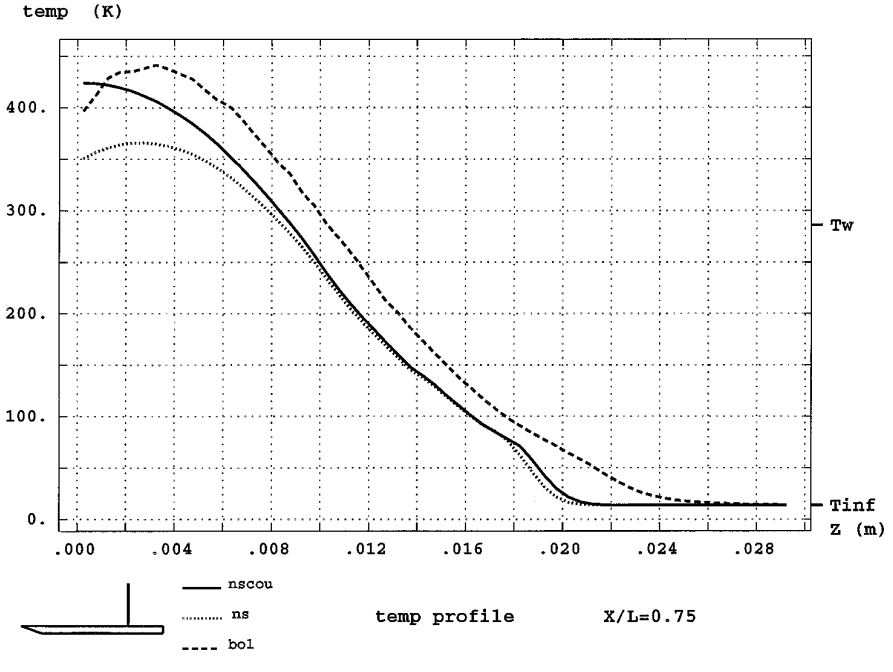

FIG. 16. Plate problem: Temperature profiles predicted by the global Boltzmann solver, by the coupled Navier–Stokes solver, and by a global Navier–Stokes solver with linear slip boundary conditions.

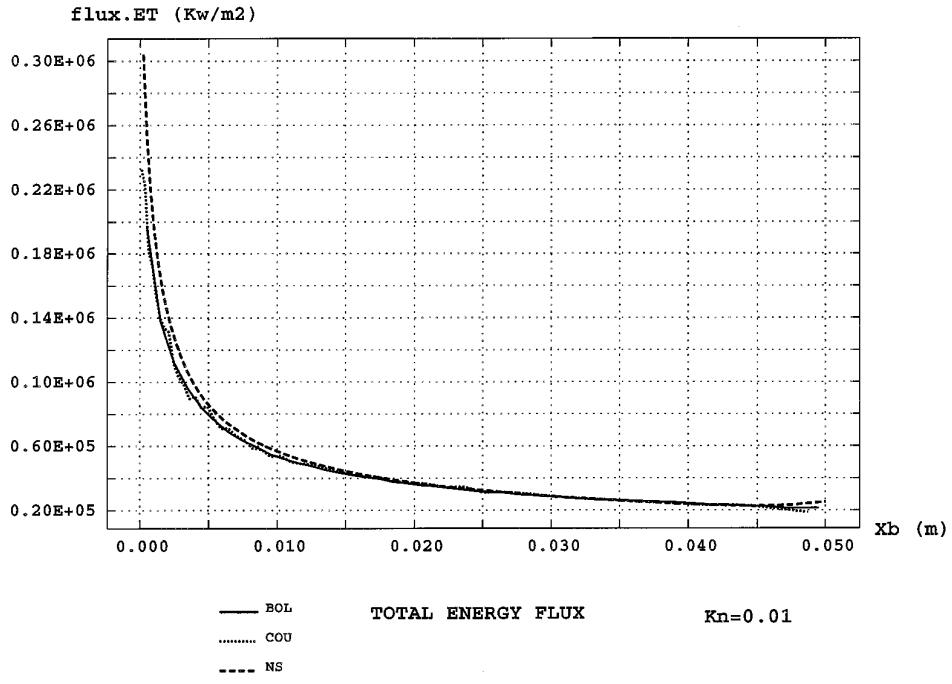

FIG. 17. Plate at an angle of attack. Wall values of the total energy flux for the three approaches in the dense case ($Kn = 0.01$): Boltzmann, Navier–Stokes, and coupled.

model (either global or coupled local), by the coupled Navier–Stokes solver or by the global Navier–Stokes solver take three different values and may differ by a factor of 2.

In summary, in the present case at no angle of attack, the coupled model represents accurately the internal structure of the global kinetic solution or of the experimental solution, provided that we use the information given by the local kinetic solver.

7.3. *Flat Plate at an Angle of Attack*

The last experimental result compares our coupled strategy to a full kinetic simulation in the case of a two-dimensional flow past a 5-cm flat plate at a 10° angle of attack. The case studied corresponds to the following data:

Mach number at infinity = 18.31,

Temperature at infinity $T_\infty(K) = 13$,

Temperature at the body $T_W(K) = 286$,

Vitesse $V_\infty(m/s) = 1477$.

We compare here the results of the coupled approach with those of a full kinetic simulation and to a Navier–Stokes calculation with linear slip boundary conditions, for a monoatomic gas with a hard sphere collision model. The Reynolds number is successively taken as Re/m = 60362 corresponding to a rather dense Knudsen number of Kn = 0.01 (Figs. 17–20) and Re/m = 7545 (rarefied Knudsen number Kn = 0.08) (Figs. 21–23).

The full kinetic simulation in the dense case (resp. rarefied case) was performed on a rectangular domain of 0.06×0.018 m (resp. 0.06×0.034 m) discretized in 20764 (resp. 10200) rectangular cells, using approximatively 660000 (resp. 315000) particles, 7000 (resp. 4500) total time steps including 6000 (resp. 4000) time steps for the accurate calculation of flow averages. The corresponding CPU time was of more than 20 h (resp. 5 h 30 min) on a HP735 workstation.

The global Navier–Stokes solution with slip boundary conditions was calculated on an adaptively refined mesh

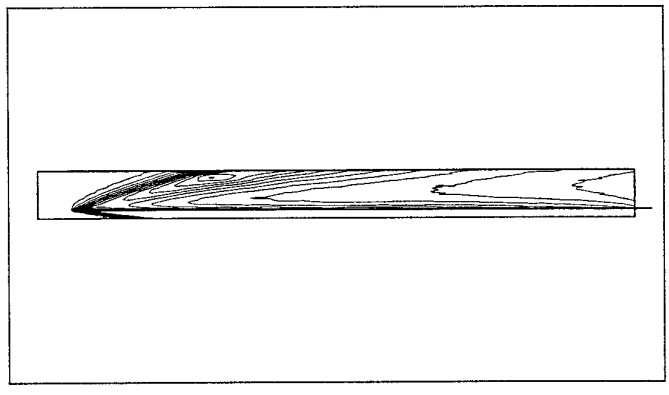

FIG. 18. Plate at an angle of attack. Isodensity lines as predicted by the local Boltzmann model in the dense coupled case ($Kn = 0.01$).

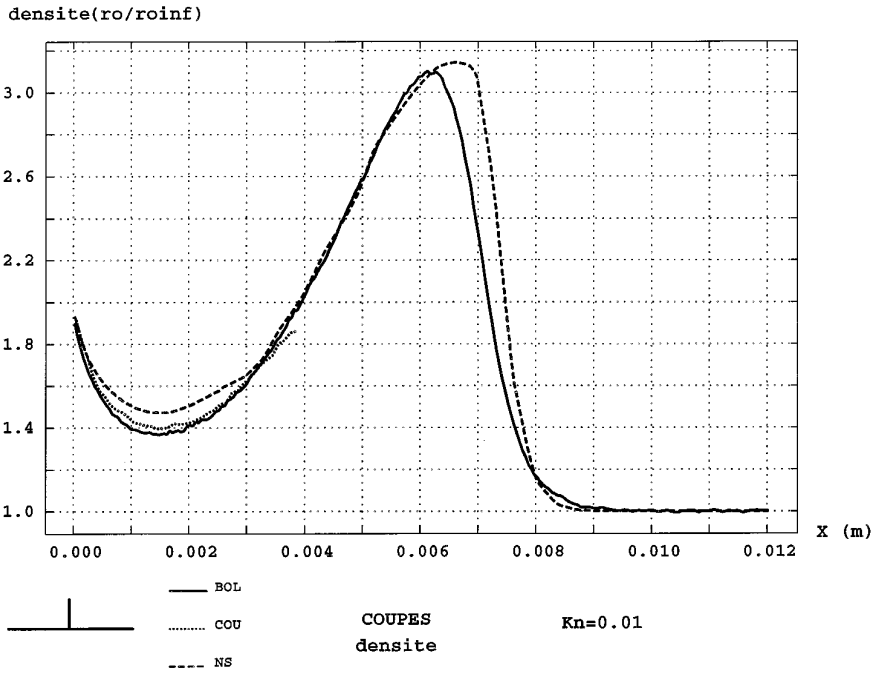

FIG. 19. Plate at an angle of attack. Density profiles for the three approaches in the dense case ($Kn = 0.01$): Boltzmann, Navier–Stokes, and kinetic coupled solution.

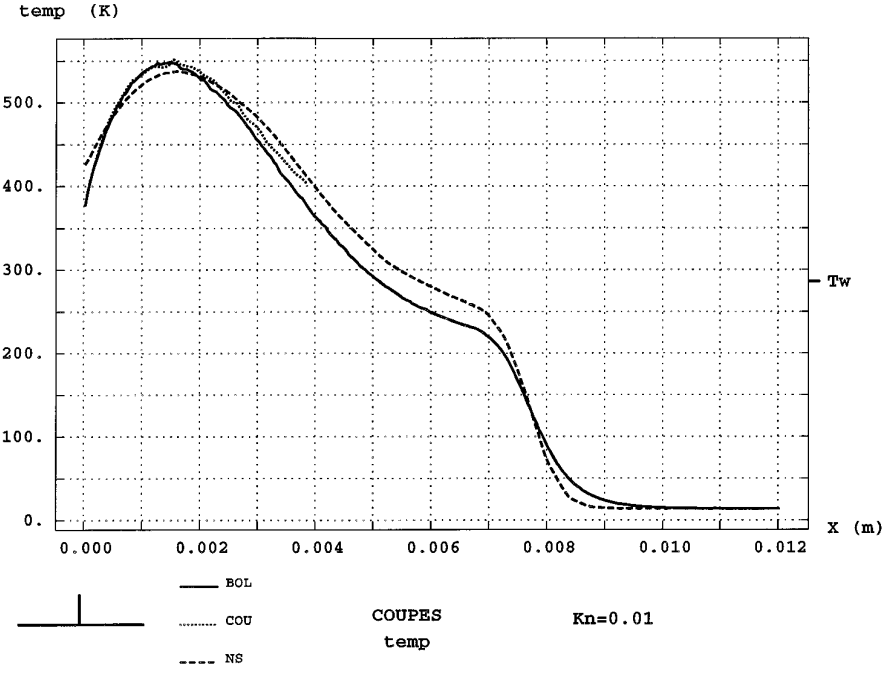

FIG. 20. Plate at an angle of attack. Temperature profiles for the three approaches in the dense case ($Kn = 0.01$): Boltzmann, Navier–Stokes, and coupled. Observe here a small difference in the temperature jump predicted by the linear slip boundary conditions and by the coupled kinetic approach.

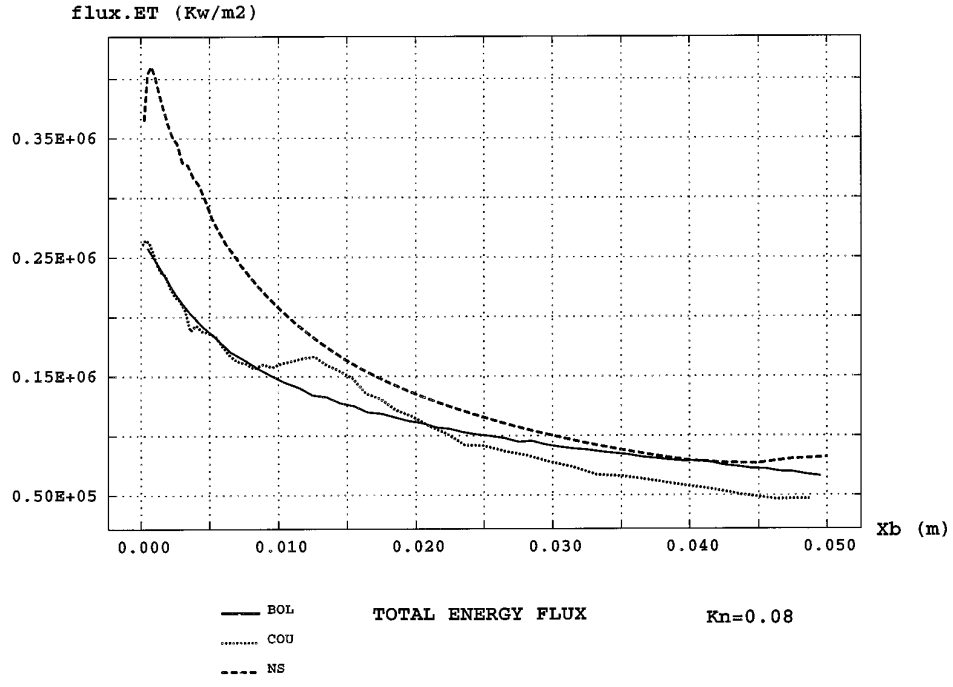

FIG. 21. Plate at an angle of attack. Wall values of the total energy flux for the three approaches in the rarefied case ($Kn = 0.08$): Boltzmann, Navier–Stokes, and coupled.

of 10668 nodes (resp. 1800 nodes) and was obtained after 10000 explicit steps.

The coupled calculations are initialized by the global Navier–Stokes solution with linear slip boundary conditions and keep the same global mesh for the Navier–Stokes part of the coupled calculation. The local Boltzmann domain is a 0.055×0.005 square box discretized in 2544 (resp. 2484) rectangular cells and using 80000 (resp. 110000) particles. We have performed three coupling iterations, each iteration consisting of 2000 (resp. 500) time steps for the local Boltzmann problem and of 1000 time steps for the global Navier–Stokes problem.

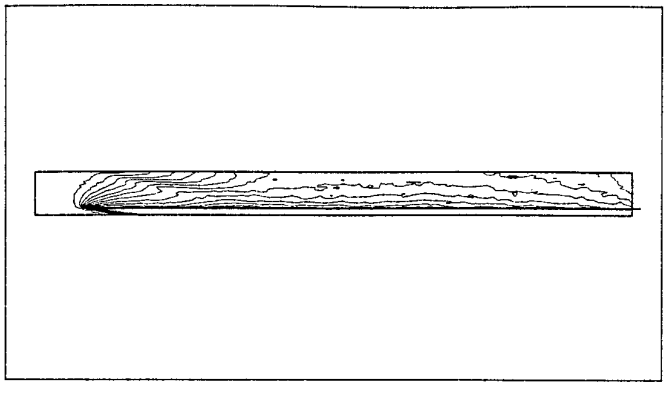

FIG. 22. Plate at an angle of attack. Isodensity lines as predicted by the local Boltzmann model in the rarefied coupled case ($Kn = 0.08$). Observe the influence of the Navier–Stokes solution as soon as the shock crosses the interface.

We present successively the values of the total energy flux at the wall, the isodensity lines as computed in the local Boltzmann approach and density or temperature profiles.

In the dense case, all three approaches yield almost identical results. We can nevertheless observe a slight discrepancy between the global Boltzmann and Navier–Stokes solutions both on the energy flux and on the density or temperature profiles. This is very likely due to the physical inaccuracy of the linear slip boundary used for Navier–Stokes. On the other hand, the coupled solution reproduces exactly the behavior of the full kinetic solution.

For a denser case run at Knudsen Kn = 0.006, all three models gave almost identical results. For the more rarefied case, however (Kn = 0.08), Navier–Stokes and Boltzmann simulations yield very different results, and this discrepancy can no longer be recovered by the coupled approach. We clearly see on the different results how the improper Navier–Stokes boundary conditions imposed at the interface affect the behavior of the local Boltzmann solution at the wall after the first fifth of the plate. In such a situation, the coupled approach is no longer valid. It could be made more accurate by increasing the size of the local Boltzmann domain, but then the coupled approach is not competitive with respect to a full kinetic simulation.

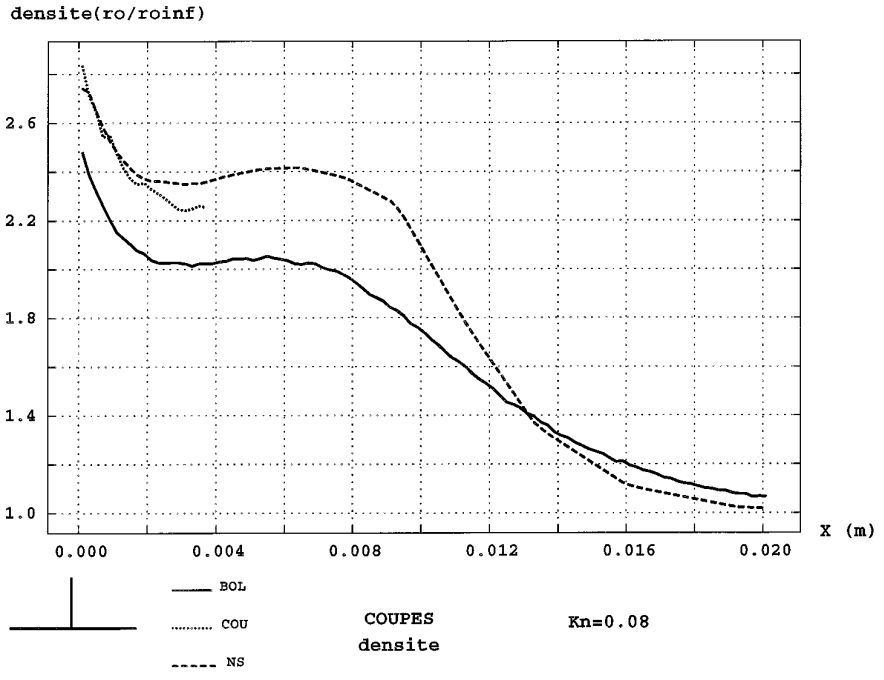

FIG. 23. Plate at an angle of attack. Density profiles for the three approaches in the rarefied case ($Kn = 0.08$): Boltzmann, Navier–Stokes, and coupled.

As a last test, we have rerun the dense calculation with a coupled approach using a local Boltzmann domain which was two times smaller (0.055×0.0025). The wall friction values are represented on Fig. 24. In this situation, the local domain appears to be a bit too small. The introduction of incoming Maxwellian distributions at the interface slightly perturbs the density next to the interface and results in a small diminution of the friction coefficient downstream.

8. CONCLUSIONS

This numerical test performed in this study confirm the validity of the Boltzmann/Navier–Stokes strategy realized herein by using friction boundary conditions.

We highlighted in this work the convergence of the method and the good agreement of the results obtained by our strategy and those obtained by a direct kinetic simulation for transitional regimes. The advantage of the proposed coupled strategy is to be applicable in situations where the direct Boltzmann simulation is not possible (because of the lack of memory place and computer power).

The coupling strategy allowed also the treatment of experimental situations in the transitional regimes and for two-dimensional gas flows. The results obtained are compatible with available experimental results and lead to the determination of a realistic accommodation coefficient at the body.

The difficulties met in this study are of two types:

First, the CPU time of the coupling approach is large. It requires more than twice the CPU time needed for a direct Navier–Stokes simulation. However, the latter fails for more complex physical situations, while the proposed strategy works well.

Second, the Navier–Stokes calculations performed within the coupling strategy required robust solvers and adequate meshes.

Finally, the domain of validity of the coupled approach is hard to identify. When the gas is too dense ($Kn \leq 10^{-4}$), the coupled approach does not bring any improvement, compared to Navier–Stokes models used with linear slip boundary conditions, but it validates these linear slip boundary conditions. When the gas is too rarefied ($Kn \geq 0.510^{-1}$), the coupling is inaccurate. When the local domain is too small, the assumption of local equilibrium on the incoming distribution slightly perturbs the wall values of friction and heat flux.

In order to circumvent those difficulties, the coupling of Navier–Stokes with Boltzmann on nonoverlapping domains using an adaptive definition of the Boltzmann domain and half fluxes interface matching is presently studied (see [3, 16]).

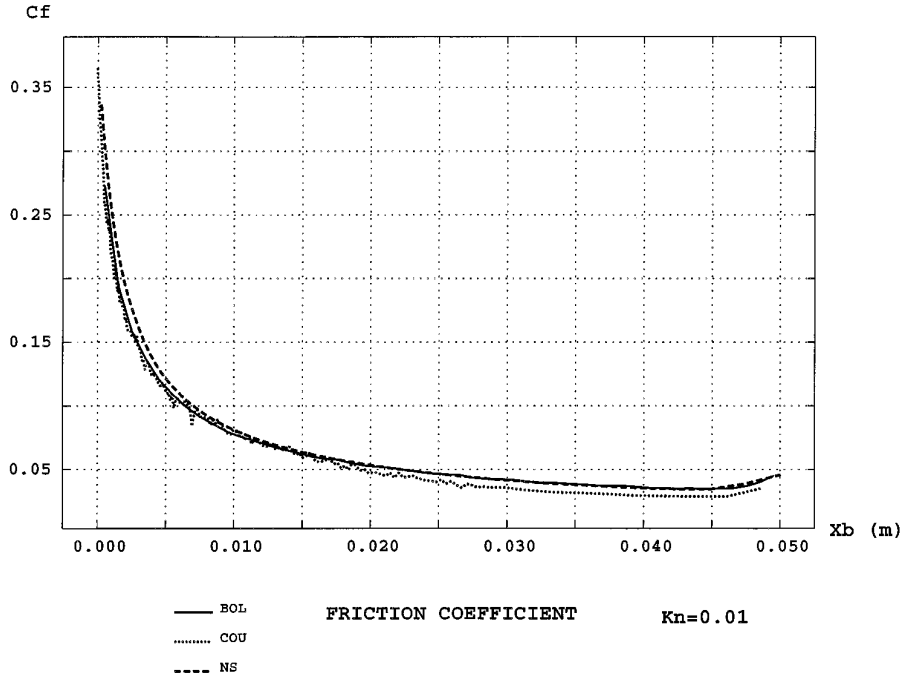

FIG. 24. Plate at an angle of attack. Wall values of the friction coefficient for the three approaches in the dense case with a small local kinetic domain ($Kn = 0.01$): Boltzmann, Navier–Stokes, and coupled. Downstream, the coupled friction is a bit smaller than both the Boltzmann and the Navier–Stokes values.

REFERENCES

1. J. Allégre, M. Raffin, J. C. Lengrand, A. Chpoun, and L. Gottesdiener, Laboratoire d'Aerothermique Report RC-89-06, Septembre 1989 (unpublished).
2. H. Babovsky, *Math. Methods Appl. Sci.* **8,** 223 (1986).
3. J. F. Bourgat, P. Le Tallec, F. Mallinger, Y. Qiu, and M. D. Tidriri, "Numerical coupling of Boltzmann and Navier–Stokes," In *Proceedings Sixth I.U.T.A.M.* (*International Union of Theoretical and Applied Mechanics*) *Conference on Rarefied Flows for Reentry Problems, Marseille, France, September 1992* (unpublished).
4. J. F. Bourgat, INRIA Technical Report 142, December 1992 (unpublished).
5. J. F. Bourgat, L. Desvillettes, P. Le Tallec, and B. Perthame, *Europ. J. Mech. B Fluids* **13,** No. 2, 237 (1994).
6. C. Borgnakke and P. S. Larsen, *J. Comput. Phys.* **18,** 405 (1975).
7. R. Brun, *Transport et relaxation dans les écoulements gazeux* (Masson, Paris, 1986).
8. C. Cercignani, *The Boltzmann equation and its applications*, Appl. Math. Sci., Vol. 67 (Springer-Verlag, New York/Berlin, 1988).
9. F. Coquel and M. S. Liou, report, Nasa Lewis Research Center (unpublished).
10. F. Coron, Thèse, Université de Paris Nord, avril 1989.
11. R. Gupta, C. Scott, and J. Moss, NASA Technical Paper 2452, November 1985 (unpublished).
12. H. Hollanders and G. Rollin, Rapport ONERA 13/3637 AY, May 1991 (unpublished).
13. J. C. Lengrand, J. C. Heffner, and A. Chpoun, Laboratoire d'Aerothermique, Report RC-90-08, Decembre 1990 (unpublished).
14. P. Le Tallec and M. D. Tidriri, submitted.
15. P. Le Tallec, M. D. Tidriri, Hermes contract report, December 1993 (unpublished).
16. P. Le Tallec and F. Mallinger, "Couplage Boltzmann Navier–Stokes," in *Proceedings*, 57th Meeting between Theoretical Physics and Mathematics, Université Louis Pasteur, December 1993" (unpublished).
17. A. Lukshin, H. Neunzert, and J. Struckmeier, *Interim Report for the Hermes Project DPH* 6174/91: *Coupling of Navier–Stokes and Boltzmann Regions*, 1992 (unpublished).
18. M. Mallet, Ph.D. thesis, Stanford University, 1985 (unpublished).
19. H. Neunzert and J. Struckmeier, "Particle Methods for the Boltzmann Equation," in *Acta Numer. 1995, Cambridge, 1995* (unpublished).
20. B. Perthame, *SIAM J. Numer. Anal.* **29,** 1 (1992).
21. Ph. Rostand and B. Stoufflet, Rapport de recherche, INRIA No. 863, Juillet, 1988 (unpublished).
22. Y. Saad and M. H. Schultz, *SIAM J. Sci. Stat. Comput.* **7,** 856 (1986).
23. J. Schneider, preprint, University of Kaiserslautern, 1995.
24. F. Shakib, Ph.D. thesis, Stanford University, 1988 (unpublished).
25. M. D. Tidriri, thèse, Université de Paris IX, May 1992 (unpublished).
26. M. D. Tidriri, *J. Comput. Phys.* **119,** 271–282 (1995).
27. M. D. Tidriri, INRIA Research Report 2435, Dec. 94 (unpublished).
28. W. G. Vicenti and C. H. Kruger Jr., *Introduction to Physical Gas Dynamics* (Wiley, New York, 1967).
29. X. Zhong, R. W. MacCormack, and D. R. Chapman, *AIAA J.* **31,** 6 (1993).